communications chemistry

A Nature Portfolio journal

Article

https://doi.org/10.1038/s42004-026-01943-6

Adsorption of organic donor-acceptor molecules on graphene/SiC preserves light-induced charge transfer

Masoud Mansouri [1] ✉, **Cristina Díaz** [2], **Jaime T. Alcolea-Cerdán** [3], **Nazario Martin** [3,4] & **Fernando Martín** [1,4] ✉

Identifying solid substrates that can effectively support donor-acceptor (DA) organic molecules without hindering their intrinsic charge transfer induced by ultraviolet and visible light is crucial for device fabrication and the precise control of photoinduced electric currents. Here, we demonstrate that graphene/SiC($000\bar{1}$) interfaces preserve the optoelectronic response of three DA molecules: 1-amino-4-nitrobenzene, 1-amino-6-nitro-pyrene, and 1-fluoro-6-methoxy-pyrene. Although adsorption induces a substantial renormalization of the molecular quasiparticle gaps, the corresponding charge-transfer excitation energies exhibit relatively small redshift compared to the gas-phase molecules. This is attributed to the substrate-induced screening that reduces both the quasiparticle gap and the electron-hole binding energy, leading to a partial cancellation in the excitation energy. Additionally, we show that the intramolecular charge-transfer excitons retain their character upon adsorption, suggesting graphene/SiC($000\bar{1}$) as a suitable platform for stable physisorption of DA chromophores and for enabling time-resolved studies of early-stage charge migration, opening pathways toward molecular optoelectronic architectures with minimal substrate interference.

Light-induced intramolecular charge transfer (ICT) between spatially separated donor (D) and acceptor (A) chemical groups plays a crucial role in natural processes such as photosynthesis, photooxidation, electronic transport, and radiation damage[1–14]. The spatial separation of these moieties often localizes the frontier molecular orbitals around the D and A groups, facilitating the dissociation of optically generated electron-hole pairs[1–4]. This process not only initiates electronic currents but also reduces recombination losses. Consequently, DA molecules are prime candidates for light-to-electricity conversion in organic photovoltaic and artificial photosynthetic devices, enhancing overall efficiency[5–8]. Furthermore, under appropriate bias voltages, DA molecules can enable resonant electron tunneling[9,10], and their directional electron flow allows them to function as molecular switches, sensors, rectifiers, and diodes[11–14].

Understanding the dynamics of electron-hole pairs generated in organic molecules ideally requires time-resolved pump-probe measurements to capture the motion of both electrons and holes in real time. In recent years, attosecond science, particularly attochemistry, has achieved the necessary time resolution to visualize ICT dynamics induced by ultraviolet (UV) and visible (Vis) radiation at the very early stages, from the first hundreds of attoseconds to tens of femtoseconds[15–20]. This is crucial not only to gain a deeper understanding of ultrafast ICT processes but also to eventually design new strategies to control them by intervening in the system immediately after ignition of the dynamics, e.g., to achieve a more efficient conversion of sunlight into electricity. Current experiments employ ultrashort (2–5 fs) UV and Vis pulses and are mostly performed in gas phase[21–24], which is optimal for direct observation of charge motion without environmental distortion but limits the scope for potential applications. Nonetheless, such experiments have the drawback of providing dynamical information averaged over all possible molecular orientations present in the gas phase, which complicates the analysis and prevents the directionality of the generated currents in the sample. To overcome these limitations, organic DA molecules should ideally be deposited on solid substrates, which are crucial for device fabrication and the control of molecular orientation. Yet, the unique charge distribution in DA molecules, characterized by regions of

---

[1]Departamento de Química, Módulo 13, Universidad Autónoma de Madrid, Madrid, Spain. [2]Departamento de Química Física, Facultad de CC. Químicas, Universidad Complutense de Madrid, Madrid, Spain. [3]Departamento de Química Orgánica I, Universidad Complutense de Madrid, Madrid, Spain. [4]Instituto Madrileño de Estudios Avanzados en Nanociencia (IMDEA Nano), Campus de Cantoblanco, Madrid, Spain. ✉e-mail: masoud.mansouri@uam.es; fernando.martin@uam.es

electron excess and deficiency, can lead to local interactions with the solid substrate, potentially altering or suppressing their optoelectronic properties.

Identifying solid substrates whose polarization dynamics do not obscure the ICT in a molecular adsorbate is vital for advancing attochemistry. Ideally, the chosen substrate should exhibit minimal interaction with a molecular adsorbate to preserve its intrinsic properties. Additionally, substrate electrons should have low mobility to minimize their interaction with external UV–Vis electromagnetic fields, thereby preventing the generation of undesired currents. This excludes metals. On the other hand, some degree of interaction is required to securely anchor a molecular adsorbate and prevent it from diffusing on the surface, which rules out most insulating substrates. In this study, we demonstrate that experimentally accessible graphene/silicon carbide interfaces[25,26] provide an effective platform for preserving the intrinsic ICT excitations of DA molecular adsorbates. Importantly, the graphene/silicon carbide substrate screens the molecular quasiparticle levels and electron-hole interactions, leaving the excitation energies and spectral features close to those of the isolated molecules in the gas phase or in solution.

Hexagonal silicon carbide (SiC) surfaces are ideal platforms for growing graphene layer(s)[25–30]. The geometry and electronic properties of the atop graphene layer are strongly influenced by the specific surface termination and stacking order of the underlying SiC[27–29]. Here, we focus on the C-terminated 6H-SiC (000$\bar{1}$) surface, shortly Si$\overline{\mathrm{C}}$, which is frequently used in device fabrication and layered heterostructures[25,26,29,30]. Unlike bulk 6H-SiC, which features a large indirect bandgap with an optical onset in the UV region, graphene-covered Si$\overline{\mathrm{C}}$ (Gr/Si$\overline{\mathrm{C}}$) exhibits a reduced bandgap and optical absorption within the visible range[29,30]. The first graphene adlayer, also called buffer layer, on the Si$\overline{\mathrm{C}}$ substrate exhibits corrugation disorder due to strong interfacial interactions, including partial covalent bonding to the surface[25,26,29,30], which suppresses the Dirac dispersion and reduces the available charge carrier densities and mobilities characteristic compared to the free-standing graphene[31].

In this work, we show that although the equilibrium adsorption geometries and quasiparticle band structures indicate that the studied DA molecules weakly interact with the Gr/Si$\overline{\mathrm{C}}$ surface, primarily through van der Waals (vdW) forces, a significant renormalization of the molecular energy levels occurs upon adsorption due to substrate-induced screening[30,32,33]. Remarkably, despite a multi-eV reduction in the highest occupied molecular orbital-lowest unoccupied molecular orbital (HOMO-LUMO) quasiparticle gap, computed absorption spectra suggest a relatively modest redshift (0.1–0.2 eV) in the molecular excitation energies compared to their gas-phase counterparts. This indicates that the substrate-induced screening that reduces the quasiparticle gap also weakens the electron-hole attraction; since the optical gap is the difference between these two many-body corrections, they partially cancel and yield the optical transition energy slightly redshifted upon adsorption[34–36]. As a result, the Gr/Si$\overline{\mathrm{C}}$ substrate strongly affects the charged excitations in the adsorbed DA molecules (i.e., excitations leading to electron removal) while the lowest neutral excitations retain their ICT character and remain energetically close to those of the isolated molecules.

Results and discussion

We have considered three DA molecules: 1-amino-4-nitrobenzene (commonly known as para-nitroaniline, PNA), 1-amino-6-nitro-pyrene (ANP), and 1-fluoro-6-methoxy-pyrene (FMP), as illustrated in the upper panels of Fig. 1. While PNA is commercially available, we have synthesized the other two molecules as elaborated in the Methods. This choice of molecules allows us to explore different ICT scenarios: PNA and ANP share the same donor ($-NH_2$) and acceptor ($-NO_2$) groups but differ in the size of their central frameworks, while ANP and FMP share the same aromatic hydrocarbon structure (four fused benzene rings) but differ in their DA substituents. In general, $-NH_2$ and $-NO_2$ groups have a stronger D and A characteristics, respectively, than $-OCH_3$ and –F, so one can expect more pronounced ICT in PNA and ANP than in FMP[14]. This is further confirmed by the UV–Vis absorption spectra shown in Fig. 1, obtained by dissolving the molecules in nonpolar hexane to approximate gas-phase conditions.

The lowest excitation of PNA, whose frontier orbitals are spatially separated between DA moieties (see Supplementary Fig. 7), is an ICT state and appears at 3.88 eV (319 nm) in UV–Vis measurements[1,2,37]. ANP exhibits a similar push-pull electronic structure, with frontier orbitals additionally involving the pyrene core. Its lowest excitation is likewise an ICT (HOMO → LUMO) state, occurring in the blue region of the visible window (435 nm, 2.85 eV). Notably, both PNA and ANP molecules exhibit pronounced solvent-polarity-dependent shifts (Supplementary Note S1), as the typical signature of ICT excitations[14]. In contrast, FMP with weaker DA substituents shows a substantial contribution from the central pyrene core in the frontier orbitals, as shown in Supplementary Note S2. Consequently, its lowest excitation at the violet edge of the visible spectrum (387 nm,

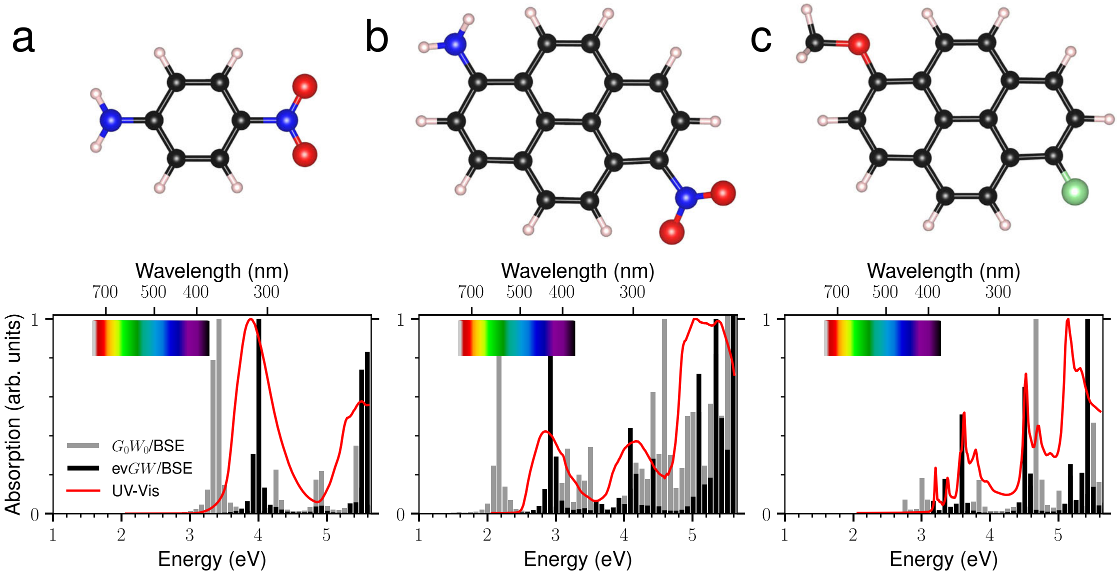

Fig. 1 | Three DA molecules and their optical absorption spectra. Molecular structures and gas-phase absorption spectra of isolated **a** PNA, **b** ANP, and **c** FMP. Black, blue, red, green, and pink circles represent C, N, O, F, and H atoms. The lower panel shows the BSE-resolved absorption lines using the quasiparticle energies obtained via G_0W_0@PBE (gray bars) and evGW (black bars), averaged over the three Cartesian coordinates, compared to the experimental UV–Vis absorbance spectrum (red curve), measured in hexane solvent.

3.2 eV) contains a more localized π-π transition, spanning over the conjugated core, mixed with a small ICT component (Supplementary Table 2)[3,38]. This is indeed in agreement with its polarity-independent absorption profile in different solvents.

Recent theoretical studies[30,32,33,35] have emphasized the importance of employing many-body perturbation theory (MBPT), including Hedin's *GW* corrections[39], to accurately capture dynamical electron-correlation effects in hybrid molecule/surface systems. This approach is essential not only for representing the electronic structure of the Gr/Si$\overline{\text{C}}$ interface but also to account for surface-induced screening (image-charge) effects on the energy levels of molecular adsorbates[32,33]. However, applying this level of theory to molecule-surface systems remains challenging due to the broken translational symmetry, requiring large supercells to precisely capture molecule-substrate interactions and minimize periodic boundary effects. In this work, we overcome these challenges by employing the one-shot *GW* (G_0W_0) scheme followed by the solution of the Bethe-Salpeter equation (BSE)[40] to accurately estimate the quasiparticle electronic structure, level alignment, and optical absorption spectra of the selected DA molecules adsorbed on Gr/Si$\overline{\text{C}}$ (see Methods).

To benchmark the methodology, we begin by comparing the UV–Vis spectra measured in solution with those calculated using the G_0W_0/BSE method in the gas phase, as shown in Fig. 1. Additionally, we include the quasiparticle spectra and optical absorption lines derived from the eigenvalue-only self-consistent *GW* method, followed by the BSE (ev*GW*/BSE). The ev*GW* approach, which minimizes starting-point dependence by iteratively updating quasiparticle eigenvalues until self-consistency is achieved in the energy levels, is widely known to provide the most accurate estimations of frontier orbital energies and the HOMO-LUMO gap in organic molecules[30,40–43]. The computed quasiparticle gaps and frontier orbital energies from ev*GW* scheme are provided in Supplementary Fig. 7. As a result, the ev*GW*/BSE results in Fig. 1 align well with the experimental UV–Vis absorption spectrum in the region where measurements have been performed. A quantitative comparison between these theoretical spectra (in gas phase) and UV–Vis spectra (in hexane solvent) reveals a maximum deviation of 0.1 eV (see Supplementary Table 1 for numbers), with a slight shift in the experimental peak positions likely arising from solvent-induced environmental effects. Notably for our current interests, the G_0W_0/BSE spectra in Fig. 1 also qualitatively reproduce the experimental line shape, relative intensities, and the separation between the main absorption bands. However, the lowest neutral excitations are underestimated by ~0.6–0.8 eV for all three molecules, reflecting the dependence of the one-shot G_0W_0 scheme to the semi-local Perdew–Burke–Ernzerhof (PBE) starting point[43] (see the corresponding quasiparticle spectra in Supplementary Fig. 7). Given these results and the high computational cost of the ev*GW* method, which prevents its applicability to large solid-state systems containing hundreds of atoms, all absorption spectra of DA molecules adsorbed on Gr/Si$\overline{\text{C}}$ have been obtained by using the G_0W_0/BSE methodology (hereafter referred to as *GW*/BSE). Importantly, the potential appearance of a small redshift in the spectra intrinsic to this methodology should not affect the comparison between the gas-phase and condensed-phase results, as both are computed consistently at the same level of theory, ensuring a clear assessment of adsorption-induced changes.

As an illustration, Fig. 2a depicts the configuration of a DA molecule adsorbed onto the Gr/Si$\overline{\text{C}}$ interface. For each adsorbate, several possible adsorption sites were considered along both the zigzag and armchair directions of the underlying graphene. After full structural relaxation, the most energetically favorable configuration was identified, as detailed in Supplementary Note S4. In the optimized geometries, the equilibrium

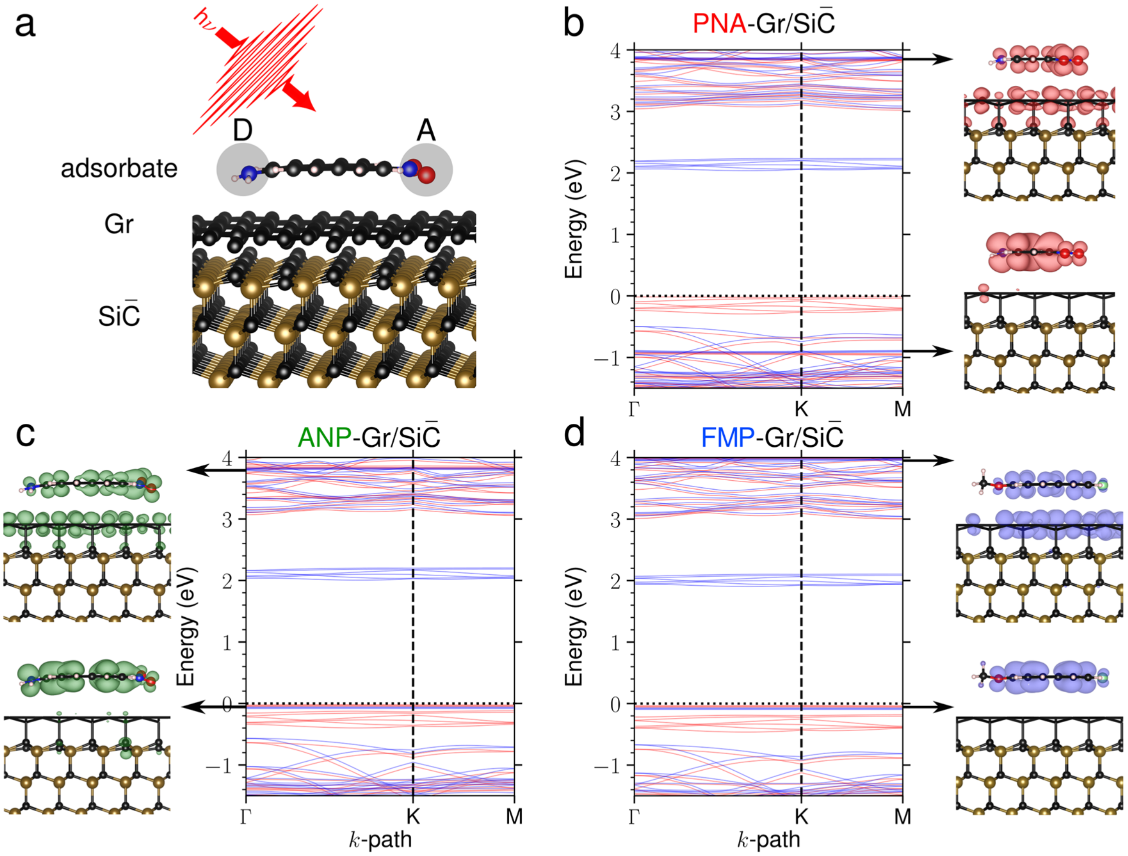

Fig. 2 | Adsorption model and electronic structure of the studied DA molecules on Gr/Si$\overline{\text{C}}$. a An illustration of the optimized configuration of the DA molecule adsorbed on the Gr/Si$\overline{\text{C}}$ system. **b–d** Quasiparticle band structures of PNA, ANP, and FMP molecules adsorbed on Gr/Si$\overline{\text{C}}$, respectively. The majority and minority spin channels are shown in red and blue, with the VBM of the molecule-substrate system set to zero energy. The spatial distribution of the states associated with the HOMO and LUMO of the adsorbate shows the degree of hybridization.

distance between the molecular backbone and graphene is ~3.4 Å, with the DA functional groups bending toward the surface by 0.2–0.6 Å (Supplementary Fig. 12). This aligns with the computed adsorption energies[44] for PNA, ANP, and FMP, which are −0.59, −1.06, and −0.72 eV, respectively. These results suggest that ANP and FMP, with their more extended structures compared to PNA, are more polarizable, while the stronger interaction of anchoring DA groups in the ANP adsorbate indicates a more energetically favorable adsorption compared to FMP. For the three adsorbates, Bader charge analysis indicates a slight excess charge of 0.05–0.15 |e|, donated from the underlying graphene and mainly accumulated on the acceptor ligands (see charge density maps in Supplementary Fig. 13). Given these results, it implies that the studied DA molecules provide a stable physisorption mechanism with typical vdW coupling and slow charge-transfer rates in the tunneling/Marcus regime[45]. This is further confirmed by inspecting the orbitals and quasiparticle band structures in Figs. 2b–d, showing that the HOMO of the adsorbate in all three systems is only slightly hybridized with the substrate states. Within the quasiparticle band structures, one also observes modifications in the molecular energy levels, most notably a renormalization of the HOMO-LUMO gap upon adsorption[29,30,33]. As indicated in the corresponding band structures, the quasiparticle HOMO-LUMO gaps of the PNA, ANP, and FMP adsorbates are ~4.8, 3.8, and 4.0 eV, respectively. In contrast, the gaps of the free-standing DA molecules, computed at the same *GW*@PBE level of theory, are 7.10, 5.01, and 5.97 eV, respectively (see Supplementary Fig. 8). These multi-eV reductions in the HOMO-LUMO gap of the adsorbates highlight the surface-induced screening effects (monopole screening) that lower the energy cost of the addition or removal of an electron from the molecular adsorbate[32,33,35]. Notably, although PNA and ANP contain identical DA substituents, their quasiparticle gap renormalizations differ due to the distinct spatial character of their frontier orbitals and their intrinsic polarization. In PNA, the HOMO and LUMO are relatively compact and carry significant weight on the substituents, enhancing image-charge stabilization and leading to the largest renormalization. In contrast, ANP, with more delocalized frontier states extended over the pyrene core and stronger intrinsic polarization, exhibits reduced sensitivity to substrate screening. Similarly, FMP with delocalized frontier orbitals but weaker DA asymmetry experiences a renormalization magnitude intermediate between those of PNA and ANP.

Figure 3 a presents the absorption spectra of PNA, ANP, and FMP molecules adsorbed on Gr/Si$\overline{\text{C}}$, calculated using the BSE approach based on *GW*@PBE quasiparticle corrections. These spectra are compared to the absorption spectrum of the pristine substrate (gray-shaded region), which was also obtained at the same level of theory. Although the spectra are shown in arbitrary units, the relative intensities are consistent across all cases. A visual inspection of Fig. 3a reveals that, for all three DA molecules, the excitations driven by the adsorbate are clearly distinguishable from the substrate background. Furthermore, inspecting the excitonic wavefunctions confirms that the molecular-derived excitations retain their ICT character and remain mainly confined within the molecular framework. This indeed demonstrates that Gr/Si$\overline{\text{C}}$ serves as an excellent support for the adsorption of the studied DA molecules, without compromising their intrinsic optical properties or ICT characteristics. Importantly, although the quasiparticle band structures in Fig. 2b–d show a substantial substrate-induced renormalization of the molecular HOMO-LUMO gaps (on the order of 1.2–2.3 eV), the lowest optical excitations of the adsorbed molecules undergo a redshift of only 0.1–0.2 eV relative to the corresponding excitations in the gas phase (dashed lines in Fig. 3a; full gas-phase spectra in Supplementary Fig. 8). These redshifts are typically smaller than the energy differences between the electronic states of the considered molecules, so it would be expected that the charge dynamics after excitation by broadband light pulses would be qualitatively similar to that observed in the gas phase[18,20]. Additionally, the redshifts in the optical spectra reflect the fact that Gr/Si$\overline{\text{C}}$ screening affects the monopolar charged excitations more strongly than the dipolar electron-hole pairs[34,36]; while screening stabilizes the charged quasiparticle states and thus strongly renormalizes the HOMO-LUMO gap, it weakens the electron-hole interaction in the neutral excitation to a lesser extent. Because these many-body corrections enter the optical gap with opposite signs, they partially cancel, resulting in only a small redshift of the excitation energies[35,36]. Therefore, the lowest adsorbate-derived excitation on Gr/Si$\overline{\text{C}}$ not only preserves the photochemical behavior of the isolated molecules but also remains close to the lowest excitation energy in the free-standing spectrum. It is important to emphasize that the optical characteristics discussed above are computed by properly accounting for electron-hole interactions, as is the case of the *GW*/BSE methodology, while excluding these electron-hole interactions gives rise to different optical structures, spanning the UV region, as shown in the case of the *GW*/random-phase approximation (*GW*/RPA) in Supplementary Fig. 15.

In more detail, for the PNA molecule adsorbed on the Gr/Si$\overline{\text{C}}$ substrate, the weak vdW interaction produces a slight hybridization between the HOMO of the adsorbate and the substrate. This results in a flat band at

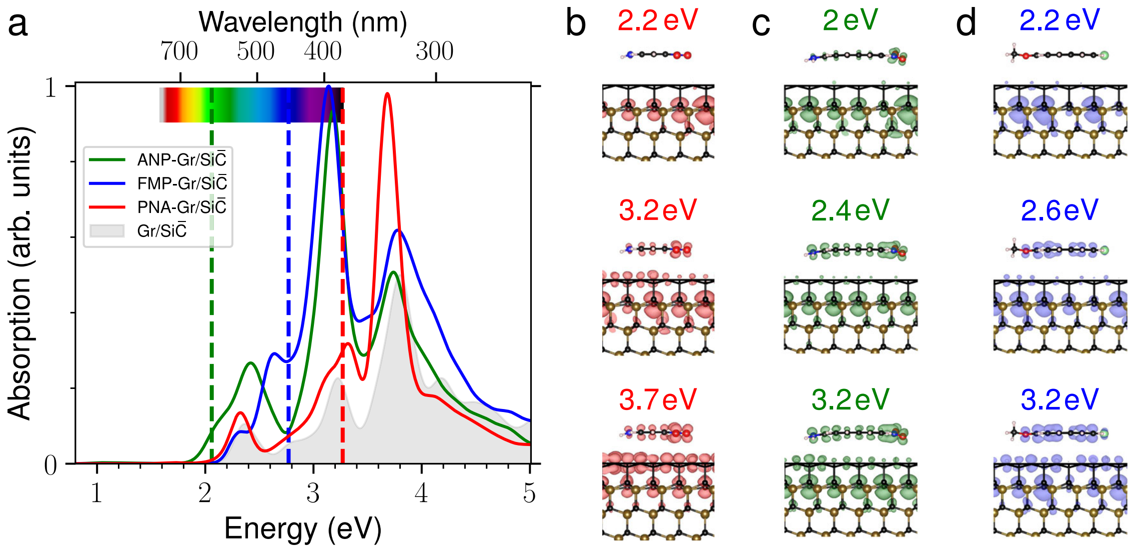

Fig. 3 | Absorption spectra of Gr/Si$\overline{\text{C}}$ with and without DA adsorption. **a** Optical absorption of the Gr/Si$\overline{\text{C}}$ surface without (shaded gray area) and with PNA (red curve), ANP (green curve), or FMP (blue curve) adsorbate. Spectra were renormalized to the highest absorption peak, and a Gaussian broadening of 0.1 eV was applied to all spectra. Vertical dashed lines represent the lowest excitation of the free-standing adsorbate at the same level of theory. **b**–**d** The isosurface of the electron density corresponding to the three BSE exciton states at the given energy, with the hole fixed on the adsorbate.

0.96 eV below the valence band maximum (VBM), as seen in the quasiparticle band structure in Fig. 2b. On the other hand, the LUMO of the PNA adsorbate appears at 3.85 eV above the VBM (at the Γ-point). As a result, the quasiparticle gap of the PNA upon adsorption is estimated to be 4.8 eV. Introduction of these molecular levels into the host band structure leads to clear differences in the *GW*/RPA spectrum of PNA/Gr/Si$\overline{\mathrm{C}}$ relative to the pristine substrate, particularly at energies near the molecular gap (Supplementary Fig. 15). When electron-hole interactions are included, the *GW*/BSE solutions suppress most of these molecular signatures at lower energies. As can be seen in Fig. 3a, below a photon energy of 3 eV, the BSE spectra of the substrate with and without PNA are similar and primarily dominated by substrate-originated transitions. However, an analysis of the exciton wavefunctions at higher energies reveals contributions from the molecular electron density, particularly transitions involving the LUMO of the PNA in the near-UV range. For example, as shown in Fig. 3b, excitations at 3.2 and 3.7 eV correspond to transitions with contributions from the LUMO of the molecular adsorbate. For comparison, the free-standing PNA molecule at the same level of theory exhibits a HOMO-LUMO quasiparticle gap of 7.1 eV, with an ICT (HOMO→LUMO) transition in the absorption spectrum appearing at 3.27 eV (see Supplementary Fig. 8 and Supplementary Table 2). Thus, one finds that despite the significantly renormalized quasiparticle HOMO-LUMO gap of PNA upon adsorption (from 7.1 eV in the gas phase to 4.8 eV on the surface), the lowest molecule-derived excitation in the BSE optical spectrum of PNA/Gr/Si$\overline{\mathrm{C}}$ remains close to that of the isolated molecule at 3.27 eV. This relatively small redshift in the optical gap of PNA upon adsorption reflects the close competition between substrate-induced screening effects on the quasiparticle gap and the exciton binding energy of the PNA adsorbate, leaving the molecular optical gap nearly surface-independent[34–36].

For the ANP molecule adsorbed on Gr/Si$\overline{\mathrm{C}}$, the quasiparticle band structure in Fig. 2c shows that the slightly hybridized HOMO of the adsorbate forms the valence edge with the LUMO at ~3.8 eV above the VBM (Γ-point). Compared to the 5.01 eV gap of the free-standing (Supplementary Fig. 8), the adsorbed ANP molecule therefore exhibits a 1.2 eV gap renormalization. Upon ANP adsorption, moreover, the absorption spectrum in Fig. 3a shows an enhanced oscillator strength in the visible range relative to the pristine substrate, with an onset at 1.94 eV and peaks at 2.4 and 3.2 eV. Exciton analysis (Fig. 3c) confirms that these states include contributions from the ANP-LUMO. For comparison, free-standing ANP features a bright ICT excitation at 2.06 eV, followed by additional transitions between 3.0 and 3.6 eV (Supplementary Fig. 8). Thus, adsorption on the Gr/Si$\overline{\mathrm{C}}$ substrate provokes a relatively small shift in the ICT of ANP, despite a 1.2 eV renormalization of its quasiparticle gap. Similarly, the HOMO-LUMO gap of FMP decreases from 5.97 eV in the gas phase to ≈4 eV upon adsorption (Fig. 2d), while the BSE absorption spectrum (blue curve in Fig. 3a) shows two distinct peaks at 2.6 and 3.2 eV, involving the LUMO and LUMO+1 of the molecule. Notably, FMP exhibits a somewhat larger redshift upon adsorption than ANP and PNA, which can be tentatively attributed to the mixed character of its lowest transition, combining localized π-π excitation with ICT, as summarized in Supplementary Table 2.

Altogether, our results indicate that the electronic structure of the Gr/Si$\overline{\mathrm{C}}$ interface is largely preserved upon adsorption of the three studied molecules. The molecules are stably physisorbed at an equilibrium distance of ~3.4 Å, with only modest charge transfer, consistent with weak vdW interactions and limited molecule-substrate hybridization. Nonetheless, surface-induced screening, i.e., image-charge effects, significantly renormalizes the adsorbate HOMO-LUMO gaps relative to the gas phase[32,33], while the corresponding optical excitations experience only a minor redshift. This behavior reflects the competing impact of the surface-induced screening on both the quasiparticle gap and the electron-hole binding energy, leading to a partial cancellation in the resulting optical gap[34,35]. Consistently, inspection of the excitonic wavefunctions confirms that the molecular-derived excitations retain their ICT character and remain confined within the molecular framework. As a result, the lowest excitons are intramolecular in nature, and their excitation energies are slightly (0.1–0.2 eV) redshifted on Gr/Si$\overline{\mathrm{C}}$.

Conclusion

We have investigated the optical properties of three donor-acceptor molecules in the gas phase and when physisorbed on the graphene/SiC(000$\overline{1}$) interface using the *GW*/BSE approach. For the isolated molecules, we have shown an excellent agreement between the UV−Vis measurements and the calculated spectra, suggesting that the lowest neutral excitations involve intramolecular charge-transfer dominated by the HOMO→LUMO transition. Upon adsorption, the band structure of the graphene/SiC(000$\overline{1}$) surface remains almost unchanged, whereas the quasiparticle levels of the molecular adsorbates undergo a modification by substrate-induced screening, with a 1.2–2.3 eV renormalization of the quasiparticle HOMO-LUMO gap. Despite this strong impact on charged excitations, the intramolecular charge transfer (neutral) excitations of the adsorbates exhibit redshifts of only 0.1–0.2 eV relative to the free-standing molecules. This relatively weak redshift reflects the close competition between substrate screening impact on the quasiparticle gap and the exciton binding energy, leaving the optical gap only slightly reduced. Additionally, the intramolecular charge transfer excitons remain confined within the molecular framework and retain the character and spectral signatures of the isolated molecules. These findings establish graphene/SiC(000$\overline{1}$) as a substrate that enables stable physisorption of DA molecules without suppressing or distorting their intrinsic low-energy excitations. Therefore, this interface holds promise for facilitating time-resolved studies of early-stage charge migration, overcoming limitations inherent in current gas-phase experiments, and paving the way to probe and manipulate ultrafast electronic dynamics in molecular optoelectronics.

Methods

Computational methods

For isolated molecules, calculations were conducted using the all-electron MOLGW code[46] with a Gaussian cc-pVQζ basis set. Alongside the perturbative G_0W_0@PBE method, we utilized the ev*GW* approach, where the quasiparticle corrections were iteratively applied until the energy gap converged to within 0.01 eV. The corresponding optical absorption lines were computed with all neutral excitations in the full diagonalization scheme. The Gr/Si$\overline{\mathrm{C}}$ surface was modeled using a C-terminated $3\sqrt{3}\times2\sqrt{3}$R30° 6H-SiC, with three bilayers, commensurated with 24 graphene unit cells and a vacuum interval of 14 Å[29,30]. For surface calculations, collinear spin-polarized DFT solutions were obtained using the QUANTUM ESPRESSO[47] package, employing the PBE functional, norm-conserving pseudopotentials[48], and a converged plane-wave cutoff of 120 Ry. Geometry optimizations were performed using the same parameters, along with the Grimme corrections[49] to account for vdW interactions, converging the total energy and inter-atomic forces to less than 10^{-4} eV and 0.01 eV per Å, respectively. The G_0W_0 quasiparticle and optical absorption spectra were computed using the BERKELEYGW package[50], treating the frequency dependence of the dielectric function within the plasmon-pole model[40]. The dielectric matrices and self-energy corrections were calculated using a Γ-centered sampling grid of $3\times3\times1$ in the Brillouin zone, an energy cutoff of 14 Ry, a Coulomb truncation scheme, and at least 3000 virtual bands, ensuring convergence of the quasiparticle gap within 0.05 eV. Optical absorption and excitonic properties were obtained by solving the BSE within the Tamm–Dancoff approximation[40,50]. To solve the BSE kernel, interpolation to a finer $9\times9\times1$ grid was performed, along with the inclusion of at least 11 valence and 15 conduction bands, ensuring coverage of molecular frontier orbitals on either side of the band gap (see the convergence of the absorption spectra in Supplementary Note S4).

Experimental methods

^{1}H NMR spectra were recorded at 300 MHz (Bruker AVIII). ^{13}C NMR spectra were recorded at 75 MHz (Bruker AVIII) and 126 MHz (Bruker AV). ^{19}F NMR spectra were recorded at 282 MHz (Bruker AVIII) and

470 MHz (Bruker AV). Chemical shifts in all cases are expressed in parts per million (ppm) relative to the solvent. ^{1}H NMR data are reported as follows: chemical shift, multiplicity (s = singlet, d = doublet, dd = doublet of doublets, m = multiplet), coupling constant (Hz), and integration. FTIR spectra were carried out in a Spectrum 3^{TM} spectrometer using a spectral range of 4000–400 cm^{-1}, with a resolution of 1 cm^{-1} and on solid samples. Mass spectrometry was carried out by electrospray ionization (ESI) on a Bruker Impact II QTOF mass spectrometer coupled to UHPLC, or considering Atmospheric Pressure Chemical Ionization Mass Spectrometry (APCI-MS) measurements on a Finnigan TSQ 7000 triple stage quadrupole mass spectrometer. UV–Vis spectroscopic measurements were conducted on a Varian Cary 5000 UV–Vis-NIR spectrophotometer using 1 cm path length quartz cells at 298 K. Emission spectroscopic measurements were performed in a Picoquant FluoTime 300 fluorescence spectrometer. See further details and the scheme of synthesizing ANP and FMP molecules in Supplementary Methods.

Data availability

All data generated and analyzed throughout this work are available from the corresponding authors upon reasonable request.

Received: 15 September 2025; Accepted: 5 February 2026;

References

1. Thomsen, C. L., Thøgersen, J. & Keiding, S. R. Ultrafast charge-transfer dynamics: studies of p-nitroaniline in water and dioxane. *J. Phys. Chem. A* **102**, 1062–1067 (1998).
2. Máximo-Canadas, M. & Borges Jr, I. Absorption spectra of p–nitroaniline derivatives: charge transfer effects and the role of substituents. *J. Mol. Model.* **30**, 120 (2024).
3. Wang, S. et al. Rational design of hybridized local and charge transfer emitters towards high-performance fluorescent blue oleds. *J. Mater. Chem. C.* **11**, 8196–8203 (2023).
4. Bergkamp, J. J., Decurtins, S. & Liu, S.-X. Current advances in fused tetrathiafulvalene donor–acceptor systems. *Chem. Soc. Rev.* **44**, 863–874 (2015).
5. Amacher, A. et al. A quinoxaline-fused tetrathiafulvalene-based sensitizer for efficient dye-sensitized solar cells. *Chem. Commun.* **50**, 6540–6542 (2014).
6. Mubarik, A., Shafiq, F., Wang, H.-R., Jiang, J. & Ju, X.-H. Theoretical design and evaluation of efficient small donor molecules for organic solar cells. *J. Mol. Model.* **29**, 373 (2023).
7. Haseena, S. & Ravva, M. K. Theoretical studies on donor–acceptor based macrocycles for organic solar cell applications. *Sci. Rep.* **12**, 15043 (2022).
8. Irfan, A. & Mahmood, A. Designing of efficient acceptors for organic solar cells: molecular modelling at dft level. *J. Clust. Sci.* **29**, 359–365 (2018).
9. Meier, T. et al. Donor-acceptor properties of a single-molecule altered by on-surface complex formation. *ACS Nano* **11**, 8413–8420 (2017).
10. Gilbert Gatty, M. et al. Hopping versus tunneling mechanism for long-range electron transfer in porphyrin oligomer bridged donor-acceptor systems. *J. Phys. Chem. B* **119**, 7598–7611 (2015).
11. Metzger, R. M. Unimolecular electrical rectifiers. *Chem. Rev.* **103**, 3803–3834 (2003).
12. He, Y., Li, N. & Brabec, C. J. Single-component organic solar cells with competitive performance. *Org. Mater.* **3**, 228–244 (2021).
13. Duan, L., Qiao, J., Sun, Y. & Qiu, Y. Strategies to design bipolar small molecules for oleds: Donor-acceptor structure and non-donor-acceptor structure. *Adv. Mater.* **23**, 1137–1144 (2011).
14. Kim, S.-Y., Kim, M.-J., Ahn, M., Lee, K.-M. & Wee, K.-R. Systematic energy band gap control of pyrene based donor-acceptor-donor molecules for efficient chemosensor. *Dyes Pigments* **191**, 109362 (2021).
15. Calegari, F. et al. Ultrafast electron dynamics in phenylalanine initiated by attosecond pulses. *Science* **346**, 336–339 (2014).
16. Lara-Astiaso, M. et al. Attosecond pump–probe spectroscopy of charge dynamics in tryptophan. *J. Phys. Chem. Lett.* **9**, 4570–4577 (2018).
17. Calegari, F. & Martin, F. Open questions in attochemistry. *Commun. Chem.* **6**, 184 (2023).
18. Vismarra, F. et al. Few-femtosecond electron transfer dynamics in photoionized donor–π–acceptor molecules. *Nat. Chem.* **16**, 2017–2024 (2024).
19. Loriot, V. et al. Attosecond metrology of the two-dimensional charge distribution in molecules. *Nat. Phys.* **20**, 765–769 (2024).
20. Mocci, D. et al. Ultrafast structural reorganization and charge dynamics in a photoionized donor-acceptor biphenyl molecule. *Ultrafast Sci.* **5**, 0108 (2025).
21. Galli, M. et al. Generation of deep ultraviolet sub-2-fs pulses. *Opt. Lett.* **44**, 1308–1311 (2019).
22. Reduzzi, M. et al. Direct temporal characterization of sub-3-fs deep uv pulses generated by resonant dispersive wave emission. *Opt. Express* **31**, 26854–26864 (2023).
23. Colaizzi, L. et al. Few-femtosecond time-resolved study of the uv-induced dissociative dynamics of iodomethane. *Nat. Commun.* **15**, 9196 (2024).
24. Wanie, V. et al. Capturing electron-driven chiral dynamics in UV-excited molecules. *Nature* **630**, 109–115 (2024).
25. Hass, J. et al. Structural properties of the multilayer graphene/$4h-\mathrm{SiC}(000\bar{1})$ system as determined by surface x-ray diffraction. *Phys. Rev. B* **75**, 214109 (2007).
26. Forbeaux, I., Themlin, J.-M. & Debever, J.-M. High-temperature graphitization of the 6H-SiC (0001) face. *Surf. Sci.* **442**, 9–18 (1999).
27. Hass, J. et al. Highly ordered graphene for two dimensional electronics. *Appl. Phys. Lett.* **89**, 143106 (2006).
28. Cavallucci, T. & Tozzini, V. Multistable rippling of graphene on sic: a density functional theory study. *J. Phys. Chem. C.* **120**, 7670–7677 (2016).
29. Mansouri, M., Martín, F. & Díaz, C. Tunable doping and optoelectronic modulation in graphene-covered 4H-SiC surfaces. *J. Phys. Chem. C.* **129**, 4155–4164 (2025).
30. Mansouri, M., Díaz, C. & Martín, F. Optoelectronic properties of electron-acceptor molecules adsorbed on Graphene/Silicon Carbide interfaces. *Commun. Mater.* **5**, 117 (2024).
31. Bolotin, K. et al. Ultrahigh electron mobility in suspended graphene. *Solid State Commun.* **146**, 351–355 (2008).
32. Neaton, J. B., Hybertsen, M. S. & Louie, S. G. Renormalization of molecular electronic levels at metal-molecule interfaces. *Phys. Rev. Lett.* **97**, 216405 (2006).
33. Garcia-Lastra, J. M., Rostgaard, C., Rubio, A. & Thygesen, K. S. Polarization-induced renormalization of molecular levels at metallic and semiconducting surfaces. *Phys. Rev. B* **80**, 245427 (2009).
34. Garcia-Lastra, J. M. & Thygesen, K. S. Renormalization of optical excitations in molecules near a metal surface. *Phys. Rev. Lett.* **106**, 187402 (2011).
35. Despoja, V., García de Abajo, F. J., Šunjić, M. & Novko, D. Quasiparticle spectra and excitons of organic molecules deposited on graphene and metallic substrates. *Phys. Rev. B* **88**, 235437 (2013).
36. Deilmann, T. & Thygesen, K. S. Important role of screening the electron-hole exchange interaction for the optical properties of molecules near metal surfaces. *Phys. Rev. B* **99**, 045133 (2019).
37. Aumiler, D., Wang, S., Chen, X. & Xia, A. Excited state localization and delocalization of internal charge transfer in branched push- pull chromophores studied by single-molecule spectroscopy. *J. Am. Chem. Soc.* **131**, 5742–5743 (2009).
38. Sun, G. et al. Effect of hybridized local and charge transfer molecules rotation in excited state on exciton utilization. *Sci. Rep.* **11**, 17686 (2021).

39. Hedin, L. New method for calculating the one-particle green's function with application to the electron-gas problem. *Phys. Rev.* **139**, A796–A823 (1965).
40. Martin, R. M., Reining, L. & Ceperley, D. M. *Interacting Electrons: Theory and Computational Approaches* (Cambridge University Press, 2016).
41. Rangel, T., Hamed, S. M., Bruneval, F. & Neaton, J. B. An assessment of low-lying excitation energies and triplet instabilities of organic molecules with an ab initio bethe-salpeter equation approach and the tamm-dancoff approximation. *J. Chem. Phys.* **146**, 194108 (2017).
42. Jacquemin, D., Duchemin, I. & Blase, X. Benchmarking the bethe-salpeter formalism on a standard organic molecular set. *J. Chem. Theory Comput.* **11**, 3290–3304 (2015).
43. Mansouri, M., Casanova, D., Koval, P. & Sánchez-Portal, D. *GW* approximation for open-shell molecules: a first-principles study. *N. J. Phys.* **23**, 093027 (2021).
44. Mahmoodi, T. & Mansouri, M. Structural effects of substitutional impurities on MoO_3 bilayers: a first principles study. *J. Korean Phys. Soc.* **69**, 1439–1444 (2016).
45. Nitzan, A. & Ratner, M. A. Electron transport in molecular wire junctions. *Science* **300**, 1384–1389 (2003).
46. Bruneval, F. et al. MOLGW 1: many-body perturbation theory software for atoms, molecules, and clusters. *Comput. Phys. Commun.* **208**, 149–161 (2016).
47. Giannozzi, P. et al. QUANTUM ESPRESSO: a modular and open-source software project for quantum simulations of materials. *J. Phys. Condens. Matter* **21**, 395502 (2009).
48. Hamann, D. R. Optimized norm-conserving vanderbilt pseudopotentials. *Phys. Rev. B* **88**, 085117 (2013).
49. Grimme, S., Antony, J., Ehrlich, S. & Krieg, H. A consistent and accurate ab initio parametrization of density functional dispersion correction (dft-d) for the 94 elements h-pu. *J. Chem. Phys.* **132**, 154104 (2010).
50. Deslippe, J. et al. BerkeleyGW: a massively parallel computer package for the calculation of the quasiparticle and optical properties of materials and nanostructures. *Comput. Phys. Commun.* **183**, 1269–1289 (2012).

Acknowledgements

We thank the Mare Nostrum Supercomputer of the Red Española de Supercomputación (BSC-RES) and the Centro de Computación Científica de la Universidad Autónoma de Madrid (CCC-UAM) for providing computational resources. This work has been supported by the European Research Council (ERC) under the European Union's Horizon 2020 research and innovation programme (grant agreement no. 951224, TOMATTO), the Ministerio de Ciencia e Innovación MICINN (Spain) through the projects PID2022-138288NB-C31 and PID2022-138288NB-C33, and the "Severo Ochoa" Programme for Centres of Excellence in R&D (CEX2020-001039-S).

Author contributions

M.M. performed the theoretical calculations, analyzed the data, and drafted the initial manuscript. J.A.-C. carried out the experiments under the supervision of N.M. All authors discussed the results. M.M., C.D., and F.M. revised the manuscript. F.M. supervised the project.

Competing interests

The authors declare no competing interests.

Additional information

Supplementary information The online version contains supplementary material available at https://doi.org/10.1038/s42004-026-01943-6.

Correspondence and requests for materials should be addressed to Masoud Mansouri or Fernando Martín.

Peer review information *Communications Chemistry* thanks the anonymous reviewers for their contribution to the peer review of this work.